This manuscript “Onset of slip partitioning under oblique-convergence within scaled physical experiments” is a non-peer reviewed preprint, which has been submitted to Geosphere
We encourage your feedback.

Michele Cooke (cooke@geo.umass.edu) corresponding author
University of Massachusetts Amherst

Kevin Toeneboehn
University of Massachusetts Amherst

Jennifer Hatch
University of Massachusetts Amherst

ONSET OF SLIP PARTITIONING UNDER OBLIQUE-CONVERGENCE WITHIN SCALED PHYSICAL EXPERIMENTS

Michele L. Cooke, Kevin Toeneboehn and Jennifer L. Hatch

Abstract

Oblique convergent margins host slip partitioned faults with simultaneously active strike-slip and reverse faults. Such systems defy energetic considerations that a single oblique-slip fault accommodates deformation more efficiently than multiple faults. To investigate the development of slip partitioning, we record deformation throughout scaled experiments of wet kaolin over a low convergence (< 30˚) obliquely-slipping basal dislocation. The presence of a precut vertical weakness in the wet kaolin impacts the morphology of faults but is not required for slip partitioning. The experiments reveal three styles of slip partitioning development delineated by the order of faulting and the extent of slip partitioning. Low convergent angle experiments (5˚) produce strike-slip faults prior to reverse faults. In moderate convergence experiments (10˚-25˚), the reverse fault forms prior to the strike-slip fault. Strike-slip faults develop either along existing weaknesses (precut or previous reverse-slip faults) or through the coalescence of new echelon cracks. The third style of local slip partitioning along two simultaneously active dipping faults is transient while global slip partitioning persists. The development of two active fault surfaces arises from changes in off-fault strain pattern after development of the first fault. With early strike-slip faults, off-fault contraction accumulates to produce a new reverse fault. Systems with early lobate reverse faults accommodate limited strike-slip and produce extension in the hanging wall, thereby promoting strike-slip faulting. The observation of persistent slip

partitioning under a wide range of experimental conditions demonstrates why such systems are frequently observed in oblique convergence crustal margins around the world.

1 Introduction

Oblique convergence often produces slip partitioned fault systems that have different slip rakes on multiple parallel striking faults instead of a single fault with oblique slip (e.g., Fitch, 1972; Jones and Wesnousky, 1992; McCaffrey, 1992; Yu et al., 1993; Haq and Davis, 1997; Tikoff and de Saint Blanquat, 1997; Burbidge and Braun, 1998; Bowman et al., 2003; McClay et al., 2004; Leever et al., 2011). Slip partitioning can occur at multiple scales within the crust, ranging from local convergence within restraining bends along strike-slip faults (e.g., Gomez et al., 2007; Fitzgerald et al., 2014; Bemis et al., 2015) to thousands of kilometers along convergent margins (e.g., Figure 1; Yu et al., 1993; Gaudemer et al., 1995; McCaffrey, 1996; Tikoff and de Saint Blanquat, 1997; Norris and Cooper, 2001). At subduction zones, slip partitioning typically involves two margin-parallel faults with a characteristic geometry: a dipping oblique-slip fault along the trench and a continental vertical strike-slip fault (e.g., Fitch, 1972). The development of two active faults within oblique convergent margins greatly increases the regional extent of seismic hazard and the interaction of slip partitioned faults can complicate hazard forecasting (e.g., Bayarsayhan et al., 1996; Eberhart-Phillips et al., 2003; King et al., 2005).

Despite abundant documentation and observation, some aspects of the evolution and maintenance of slip-partitioned systems remain unclear. Why do these fault systems employ two active faults rather than a single fault surface with oblique slip? Because work is consumed in the creation of new fault surfaces (e.g., Lockner et al., 1991; Herbert et al., 2015), fault systems with a single oblique-slip fault should be more efficient than systems with two simultaneously active faults. Furthermore, how do previously non-partitioned margins become slip-partitioned?

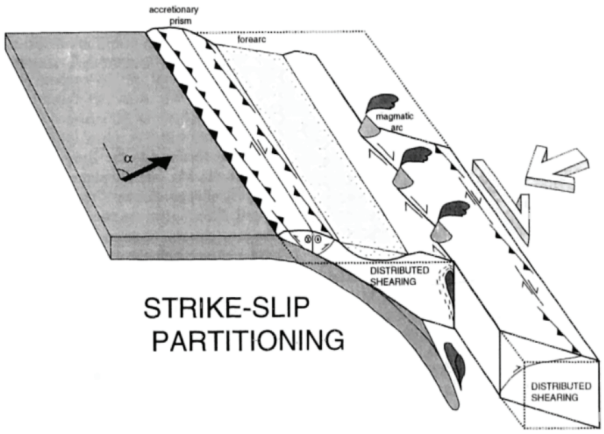

Figure 1: Example sketches of slip-partitioning at oblique convergent margins expressed as two active faults with parallel strike. The oblique subduction zone margin has reverse slip along the subduction zone and strike-slip along the inboard fault that hosts magmatic conduits (taken from Tikoff and de Saint Blanquat, 1997).

Finally, why do slip-partitioned fault systems remain so rather than shift to a single obliquely-slipping fault?

Analytical derivations that employ least-energy or force balance assumptions examine resolved stresses that drive slip along existing strike-parallel dip-slip and strike-slip faults (Michael, 1990; Jones and Wesnousky, 1992; McCaffrey, 1992; Platt, 1993). These studies, along with numerical investigations of convergent margins (e.g., Upton et al., 2003; Vernant and Chéry, 2006), shed insight into the tradeoffs in the strength of faults/interfaces and convergence obliquity that act to maintain slip partitioned fault systems but do not reveal how these systems develop. Numerical models with oblique slip on deep-seated faults highlight the asymmetry of the overlying stress field and show zones of potential faulting in the overlying crust that have distinct slip sense (Braun and Beaumont, 1995; Bowman et al., 2003). However, these numerical models do not elucidate the sequence of faulting or the mechanisms that might maintain slip partitioning.

Scaled physical experiments, with their controlled boundary conditions and known rheology, serve well to test the idealized analytical and numerical models by providing direct observations of emergent faulting (e.g., Schreurs et al., 2006; Cooke et al., 2016). Most of the previous scaled physical experiments investigating slip partitioning have used dry sand and angled basal conveyors or plates to apply oblique convergence to the overlying wedge (e.g., Richard and Cobbold, 1990; Haq and Davis, 1997, 2010; Schreurs and Colletta, 1998; McClay et al., 2004; Leever et al., 2011). Due to its low cohesion, dry sand readily forms new faults and may develop slip partitioning along two simultaneously active faults because of the low cost to grow faults in this weak material. In contrast, crustal materials have significant strength, which is ubiquitously evident by persistent slip along unfavorably oriented fault segments. Consequently, the

simultaneous development of multiple faults within dry sand may not accurately capture the sequence of faulting and the subsequent evolution of slip partitioning within crustal materials.

In this study, we use kaolin clay as a crustal analog for modeling the evolution of fault systems due to its non-zero cohesion, which facilitates the abandonment and reactivation of individual fault segments and approximates the evolution of faults in the crust (e.g., Oertel, 1965; Tchalenko, 1970; Withjack and Jamison, 1986; Ackermann et al., 2001; Eisenstadt and Sims, 2005; Henza et al., 2010; Cooke et al., 2013; Hatem et al., 2015, 2017; Bonini et al., 2016; Bonanno et al., 2017). By recording continuous high-resolution incremental displacements on discrete long-lived faults in the clay, we are able to record the evolution of slip partitioning along faults above an obliquely slipping basal discontinuity. Under convergence angles ranging from 5˚ to 25˚, the experiments both with and without a pre-existing vertical weakness demonstrate local and/or global slip partitioning.

2 BACKGROUND

Fitch (1972) first described slip partitioning as "*where slip that is oblique to the plate margin is at least partially decoupled between parallel zones of transcurrent faulting and underthrusting*". The more general term 'strain partitioning' as used in many previous studies (e.g., Burbidge and Braun, 1998; Chemenda et al., 2000; McClay et al., 2004; Gomez et al., 2007; Loveless and Meade, 2010; Leever et al., 2011), sometimes includes the decoupling of off-fault deformation, such as buckling or inferred stress orientations, from the overall plate convergence direction. In this study, we will consider only the partitioning of localized strain along faults resulting from slip.

2.1 Development of slip partitioning within oblique convergence experiments

Leever et al. (2011) used digital image correlation (DIC) to track the evolution of slip vectors along faults throughout oblique convergence experiments. This analysis shows that the slip rake of faults in dry sand changes as the system evolves. While early active faults have oblique slip, the slip vectors evolve to have greater partitioning with faults outboard of the wedge accommodating greater convergence and the fault within the wedge accommodating greater strike-slip (Leever et al., 2011). From these experiments and others (e.g., Schreurs and Colletta, 1998; McClay et al., 2004), we understand that slip partitioning might not develop at the onset of faulting under oblique convergence as considered within analytical and numerical models, but that fault systems can evolve towards slip partitioning.

Previous scaled physical experiments show that convergence angle and fault strength control the initiation and continuation of slip partitioning (Richard and Cobbold, 1990; Schreurs and Colletta, 1998; Chemenda et al., 2000; McClay et al., 2004; Haq and Davis, 2010; Leever et al., 2011). Numerical and analytical models predict that deformation partitioning in brittle materials is limited to convergence angles below ~25°-30°, measured from trench parallel (Braun and Beaumont, 1995; Burbidge and Braun, 1998; Leever et al., 2011). While experiments with dry sand over oblique conveyors confirm that strong deformation partitioning only develops when the convergence angle is less than 30° (McClay et al., 2004; Leever et al., 2011), Haq & Davis (2010), revealed that slip partitioning will develop in dry sand with convergence angles as high as 60° when the sand overlies a sliver block that provides a vertical, pure strike-slip dislocation in addition to oblique convergence dislocation. Because slip partitioning in the crust is observed at plate margins with convergence angles well above the predicted critical threshold of 30° (e.g., Dewey and Lamb, 1992; Yu et al., 1993), pre-existing weaknesses in the crust may play a key

role in the evolution of slip partitioning (e.g., De Saint Blanquat et al., 1998; Haq and Davis, 2010). Furthermore, scaled oblique convergence experiments with cohesive material overlying a viscous layer show that a pre-existing weakness is needed to produce slip partitioning under 40˚ oblique convergence (Chemenda et al., 2000). In this study, we investigate the role of a pre-existing vertical fault on the development of slip partitioning in weak but cohesive material under a range of convergence angles.

2.2 Scaling wet kaolin to the crust

Although dry sand has many benefits as an analog for modeling crustal processes (e.g. strain-rate independence, strength scaling, and ease of use, Schreurs et al., 2016), its lack of cohesion favors the growth of new faults over fault reactivation (e.g., Eisenstadt and Sims, 2005; Cooke et al., 2013). The properties of wet kaolin that produce long-lived faults are particularly important for modeling the evolution of fault systems; the abandonment and reactivation of individual fault segments in scaled physical experiments approximate the fault evolution in the crust (e.g., Clifton et al., 2000; Ackermann et al., 2001; Schlische et al., 2002; Eisenstadt and Sims, 2005; Henza et al., 2010; e.g., Hatem et al., 2015, 2017; Bonanno et al., 2017; Toeneboehn et al., 2018).

For these experiments, we follow Hatem et al. (2017) and use #6 tile clay with 5-10% sand, 30-35% silt, and 60% clay-sized particles by mass. The strength of clay can be modified by changing its water content. Following the approach of Hatem et al. (2015), we adjust the shear strength of the overlying clay to 103±3.5 Pa, which is five orders of magnitude weaker than the crust, assuming an upper crustal strength of 10-20 MPa. Since the internal friction angle of wet kaolin is similar to the crust (e.g., Schlische et al., 2002) and density ratio of the wet kaolin to crust is ~1.6:2.7 g/cm^3, the five orders of magnitude strength difference corresponds to about

five orders of magnitude scaling difference (Hubbert, 1937; Schlische et al., 2002; Henza et al., 2010; Cooke et al., 2013). Consequently, the strength ratio of wet kaolin to the crust equates 1 cm in the claybox to 1.7-3.3 km in the crust. Furthermore, rheological tests show that wet kaolin behaves as a Burger's material, similar to crustal material, with both elastic and viscous properties (Cooke and Van Der Elst, 2012). We run all the experiments of this study at the same speed, 0.5 mm/min, in order to reduce viscoelastic rate effects from the findings.

3 EXPERIMENTAL SETUP AND METHODS

For each tested convergence angle, we ran two experiments with identical boundary and loading conditions but different initial faults. One set of experiments has a precut vertical plane in the clay to simulate an existing transform margin at the onset of oblique convergence. A second set of experiments leaves the wet kaolin uncut. Both uncut and precut models simulate the development of faults loaded with oblique convergence, where a deep-seated oblique-slip fault drives the deformation of the overlying material (e.g., Bowman et al., 2003).

The block geometry in the experiments of this study creates an oblique dislocation where the center block thrusts over the footwall of the driving (i.e., subducting) block (Figure 2). Previous oblique convergence sand experiments superpose regional contraction and localized strike-slip, without capturing the dipping dislocation that characterizes oblique-convergent subduction margins (e.g., Richard and Cobbold, 1990; Haq and Davis, 2009; Leever et al., 2011). The three-dimensional displacement of the underlying rigid blocks implemented here simulates the oblique-slip dislocation where the overlying crust obliquely thrusts over the subducting slab. The experiments obliquely converge two 2.5 cm thick rigid blocks with a contact dip of 30˚ that underlie an equally thick layer of wet kaolin clay (Figure 2).

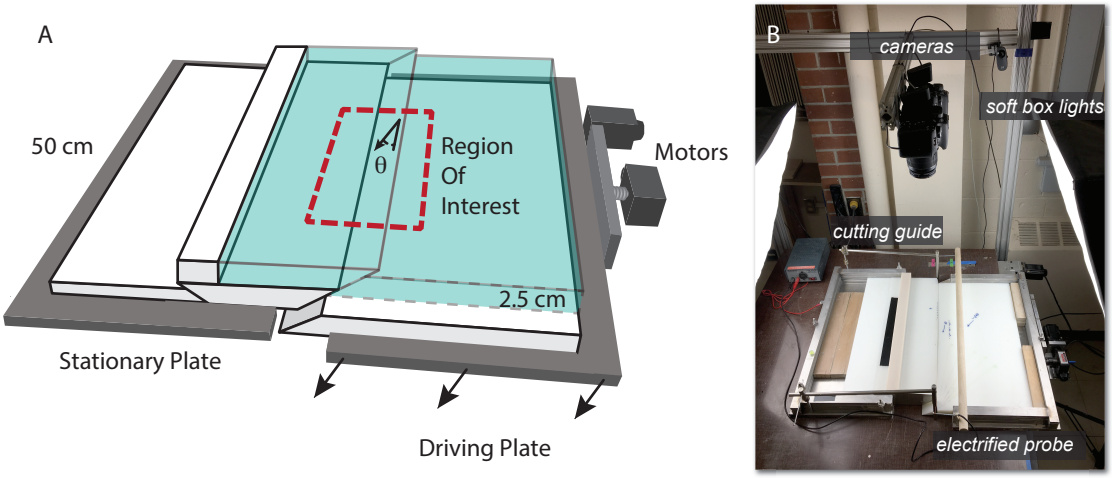

Figure 1: Schematic of model geometry depicting the three plastic blocks with abutting 30° contacts and 2.5 cm of overlying wet kaolin clay or dry sand. The blocks are positioned by two metal plates: one fixed and the other driven obliquely (, measured from margin parallel) by two 90° opposed stepper motors. (B) Two DSLR cameras mounted above the model capture high-resolution images of the region of interest (ROI) shown in the red-dashed box. To form precut surface, an electrified copper wire (24 AWG, ~0.5 mm) is stretched tight with a wooden bow (B) and used to cut a discrete vertical fault parallel to and directly above the dipping block contact before starting the motors.

157 The block above the driving plate is displaced by two stepper-motors (x- and y- axis)
158 prescribed with net velocity of 0.5±0.05 mm/min. This block drives towards the central (wedged)
159 hanging wall block that is allowed to rise along its 30˚ dipping front and back edges. The center
160 block overrides both the driving block and the fixed block and is bounded laterally by fixed
161 sidewalls. A bulls-eye level shows if the block remains level as it rises.
162 We measure the shear strength of the clay before each experiment using the Fall Cone
163 method (DeGroot and Lunne, 2007). The clay is mixed thoroughly in order to reduce
164 heterogeneities before measuring its shear strength. The depth that a 10 gram cone with 60˚ sides
165 sinks into the clay surface over a 5 second period provides an empirical estimate of undrained
166 shear strength (DeGroot and Lunne, 2007). We then adjust the water content of the kaolin to
167 achieve the desired shear strength of ~100 Pa. For the experiments in this study, the clay had a
168 water content of 81±1% by mass and shear strength of 104±1 Pa. The upper 1 cm of the kaolin
169 lost 4±1% of water over the course of the 3.5-4 hour long experiments corresponding to an
170 increase of 5-6 Pa shear strength. The bottom of the clay pack only lost 2±1% of water. For the
171 experiments with a precut vertical surface, we cut the kaolin with an electrified probe that
172 interrupts van der Waals forces and reduces puckering of the wet kaolin.
173 We document the deformation within each experiment using high-resolution digital images
174 taken every 30 seconds with a pair of Canon® EOS Rebel T3i DSLR cameras equipped with
175 standard 18-55 mm lenses. The net stepper motor movement of 0.5 mm/min means this image
176 capture rate records deformation every ~0.25 mm of driving plate displacement. The resolution
177 of the images ranges from 123-133 pixels per centimeter (Table 1). At the end of each
178 experiment, we made a trench through the faults in order to confirm the location of the basal
179 dislocation and to observe the fault dips.

Table 1: Experiment conditions

Experiment	Convergence angle mean±std	Resolution of displacements (mm)	Median net incremental displacement $\Delta \boldsymbol{u}_{tot}$ (mm)	Strain Variability (incremental strain)
05p	5.5 ±1.1˚	1.23	0.240±0.002	0.001
10p	10.2 ±2.0˚	1.23	0.228±0.003	0.001
15p	10.8±1.8˚	1.23	0.237±0.004	0.001
20p	19.3±2.3˚	1.23	0.200±0.005	0.002
25p	20.8±3.5˚	1.24	0.201±0.005	0.002
05u	5.4±1.0˚	0.91	0.235±0.006	0.002
10u	10.7±2.1˚	1.23	0.229±0.008	0.005
15u	12.3±1.6 ˚	0.94	0.223±0.005	0.003
20u	15.5±2.0˚	0.90	0.233±0.006	0.006
25u	22.5±3.0˚	1.27	0.208±0.006	0.002

Because the blocks have a width of 50 cm, the maximum lateral displacement is limited to ~27 cm to maintain a region 18 cm wide that is free of boundary effects (at least 2.5 cm margin on each side). The thickness and dip of the block contact limit the testable range of convergence to 4.33 cm. We use a 12 x 18 cm region of interest (ROI) for each experiment to capture the lateral variability in deformation.

3.2.1 Displacement Fields from Digital Image Correlation

To determine the horizontal incremental displacement field from successive photos of the deformation, we use Digital Image Correlation (DIC). DIC relies on correlating pixel constellations between each image to determine the incremental displacements. Because the clay's surface is relatively homogeneous in color and texture, we sieve high contrast red and black medium grain-sized quartz sand onto the top surface of the clay at the beginning of each experiment to provide passive markers for tracking deformation. For this study, we use the Particle Image Velocimetry (PIV) type of DIC and process the images using PIVlab (Thielicke and Stamhuis, 2014) and the Image Processing Toolbox™ from MATLAB®. Using an adaptive-iterative method (multipass) together with 50% overlapping windows, we achieve a final resolution of incremental displacement every 0.9-1.23 mm^2 (Table 1).

In addition to collecting images for horizontal displacement fields, a second high-resolution DSLR camera provides images from an alternate perspective that we use to record the three-dimensional topography throughout the experiment. We follow the stereovision technique described by Toeneboehn et al. (2018). The uplift evolution confirms the interpretations made from the horizontal incremental displacement fields measured with DIC. The resulting uplift maps are provided as supplemental material (Figures S1 and S2).

3.2.2 Fault identification and slip sense (rake)

The curl and divergence of the horizontal incremental displacement field provide spatial and temporal evolution of the strike-slip (vorticity) and contractional (-dilatational) incremental strain, respectively, at stages throughout the experiments. Since the calculation of the curl and divergence of the displacement field are independent of direction, the strains we measure are likewise independent of the orientation of the fault structures. This attribute is particularly helpful for measuring strain along the irregular fault traces; shear strain, ε_{xy}, in a global coordinate system doesn't fully capture shear strain on faults that strike oblique to x- and y- axes. We use the standard deviation of strain along a transect parallel to the block edge and far from the deforming portion of the ROI to assess the variability of the incremental strain calculated from the incremental displacement fields (Table 1). This value provides a sense of the uncertainty of the strain estimates.

Active faults are identified where the strain from the incremental horizontal displacement field, $\Delta\boldsymbol{u}$, exceeds an empirically determined threshold. At the beginning of most experiments, we press shallow parallel lines into the surface of the kaolin. Hatem et al. (2017) used the first visible detection of offset along these markers to determine a shear strain rate threshold for faulting of 0.02 radians per minute. However, this threshold depends on the velocity of the motors, which can vary slightly through the experiment, and was based only on shear strain Because we have both contraction and shear in the oblique convergence system, we need to consider both the divergence and the vorticity of $\Delta\boldsymbol{u}$. The total incremental strain sums the absolute values of both the divergence and vorticity, which is twice the curl, of $\Delta\boldsymbol{u}$ (left side of Equation 1a). Within the framework of Equation 1a, the threshold determined by Hatem et al. (2017) is equivalent to 0.08 times the net incremental displacement across the ROI, $\Delta\boldsymbol{u}_{tot}$.

Through further empirical testing, we found that this threshold works well for distinguishing initial localization of fault from distributed strain surrounding early faults but doesn't capture reactivation of existing faults, such as the reverse fault at 70 mm of plate displacement in the 5˚ convergence experiment (Figure 3). To detect localized strain along reactivated faults, we use the threshold of 0.05 times $\Delta \boldsymbol{u}_{tot}$ for experiments of this study (Equation 1b).

$$|divergence(\Delta \boldsymbol{u})| + |vorticity(\Delta \boldsymbol{u})| \geq threshold \quad (1a)$$

$$|\nabla \cdot \Delta \boldsymbol{u}| + |2(\nabla \times \Delta \boldsymbol{u})| \geq 0.05\, \Delta \boldsymbol{u}_{tot} \quad (1b)$$

Each active fault at the surface of the kaolin is manifest as a region with higher than threshold incremental strain. By using a fault threshold lower than that of Hatem et al., (2017) the early active fault zones include regions of surrounding distributed strain; however, this outcome impact neither the slip sense calculated on the faults, nor the evolution of slip partitioning investigated in this study. Once active faults are identified for each frame of the experiment, we calculate the median incremental divergence and vorticity for each fault to represent the overall slip sense of the fault within the ROI.

In order to quantify the obliquity of slip along the active faults at each stage of the experiments, we take the arctangent of the median incremental divergence divided by the vorticity of the portion of the incremental displacement field associated with each identified fault, $\Delta \boldsymbol{u}_f$. Because divergence provides positive dilatation and positive curl corresponds to left-lateral strain, we use the negative of divergence and curl for the primarily contractional and right-lateral system investigated here:

$$slip\ rake = \tan^{-1}\left[\frac{-median(\nabla \cdot \Delta \boldsymbol{u}_f)}{-2median(\nabla \times \Delta \boldsymbol{u}_f)}\right] \quad (2)$$

Using this method, a slip rake of 0˚ corresponds to a fault with pure dextral strike-slip and 90˚ corresponds to pure convergence. Faults with slip rakes between 0˚ and ±45˚ have mostly

dextral strike-slip (oblique strike-slip) with the sign indicating contraction (+) or extension (-). Slip rakes between +45˚ and +90˚ or between -45˚ and -90˚ indicate faults with mostly dip slip (i.e., oblique-reverse (+) or normal (-) faults).

4 EXPERIMENTAL RESULTS

For clarity, we describe the results from the precut and uncut experiments separately. For each suite of experiments, we present strain evolution animations for experiments that represent different styles of slip partitioning evolution. Strain evolution animations for all other experiments are available within the supplemental material (Figures S3-S8) along with uplift maps (Figures S1 and S2). Because the stepper motors do not have servo-feedback, the prescribed convergence angle is not precisely matched throughout each of the experiments. Here, we refer to each experiment by the convergence prescribed to the motors and use the DIC data to carefully measure and track the convergence experienced by the kaolin (Table 1).

4.1 Precut experiments

Across all precut experiments, slip partitioning develops along a laterally continuous sliver block bound by primarily strike-slip and reverse faults. The style of slip partitioning development varies with convergence angle. For the 5° experiment, shear strain localizes as strike-slip along the precut vertical plane early in the experiment (~5 mm net plate displacement) and later a new reverse fault develops (~40 mm net plate displacement) to produce a slip partitioned fault system (Figure 3). In contrast, within precut experiments with convergence angles >5°, a reverse fault forms first followed closely in time by strike-slip along the precut vertical fault and associated onset of slip partitioning. Figure 4 shows the incremental strain evolution of the 15˚ experiment, which is representative of the >5˚ convergence experiments.

This figure is an animation click to start

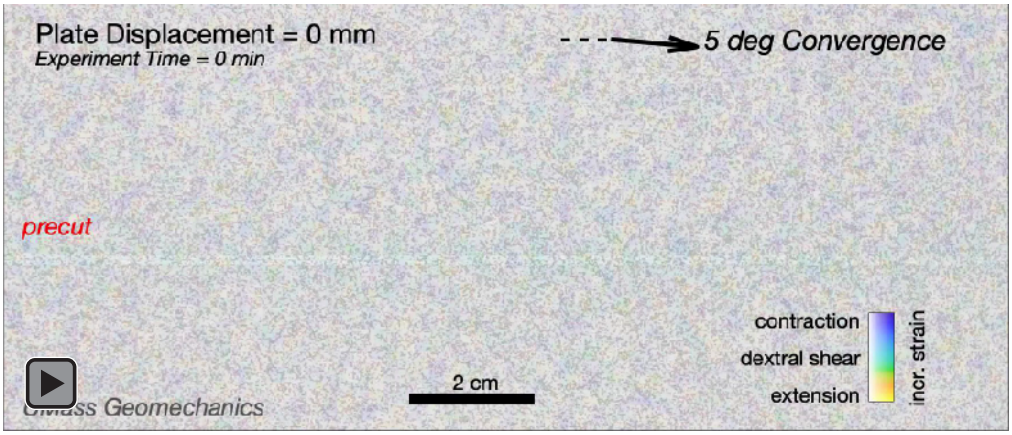

Figure 3: Animation of strain overlain on photos of the 5˚ convergence precut experiment. Hue corresponds to sense of strain and saturation reveals strain rate. For clarity the animation shows only part of the total ROI.

This figure is an animation click to start

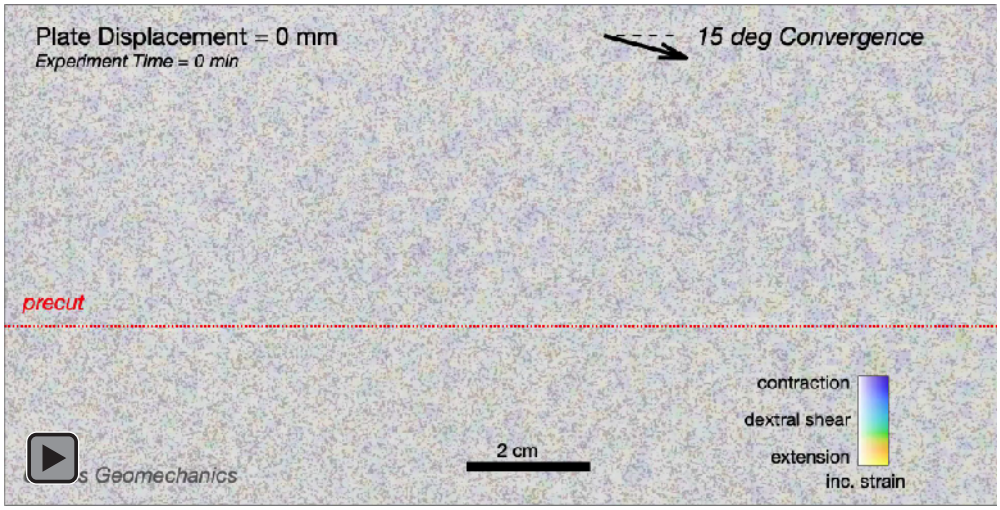

Figure 4: Animation of strain overlain on photos of the 15˚ convergence precut experiment. Hue corresponds to sense of strain and saturation reveals strain rate. For clarity the animation shows only part of the total ROI.

Early in the experiments, distributed strain starts to localize onto the new reverse faults. Even this early distributed incremental strain shows some partitioning with a zone of dextral shear closer to the hanging wall block and contraction farther from the hanging wall (~10 mm plate displacement Figure 4). This incremental strain pattern matches the analytical predictions of Bowman et al. (2003) for stress above an oblique dislocation.

As convergence accumulates along the first generation of reverse faults, a second reverse fault forms outboard of the first in all precut experiments, and the earlier set of reverse faults are abandoned. The first generation of reverse faults initiates as echelon faults. As these early segments link, they form a scalloped fault trace geometry, and the second generation of reverse faults forms lobate segments between the salients of the earlier reverse faults (Figures 3 & 4). The scalloped trace of the reverse faults also produces variable slip sense along different portions of the fault with greater or lesser incremental contraction along bends where the fault trace is oblique to the margin (Figures 3 & 4). Strike-slip along the precut surface continues throughout the development of the imbricate reverse faults.

During the reverse fault initiation, the surface of the kaolin shows a zone of early distributed incremental strain that becomes more localized over 5-10 mm of plate displacement and migrates away from the precut as it localizes (Figures 3 & 4). This strain evolution, which is supported by the uplift patterns (Figure S1), suggests that the reverse fault grows upward from the underlying dislocation between the basal blocks.

Once developed, the reverse faults show evidence for temporally variable slip rates. For both the 5° and 10° experiments, the primarily reverse fault temporarily stops slipping or has strain rates lower than the threshold for detecting slip (Figure 5). The stalled reverse faults in these two

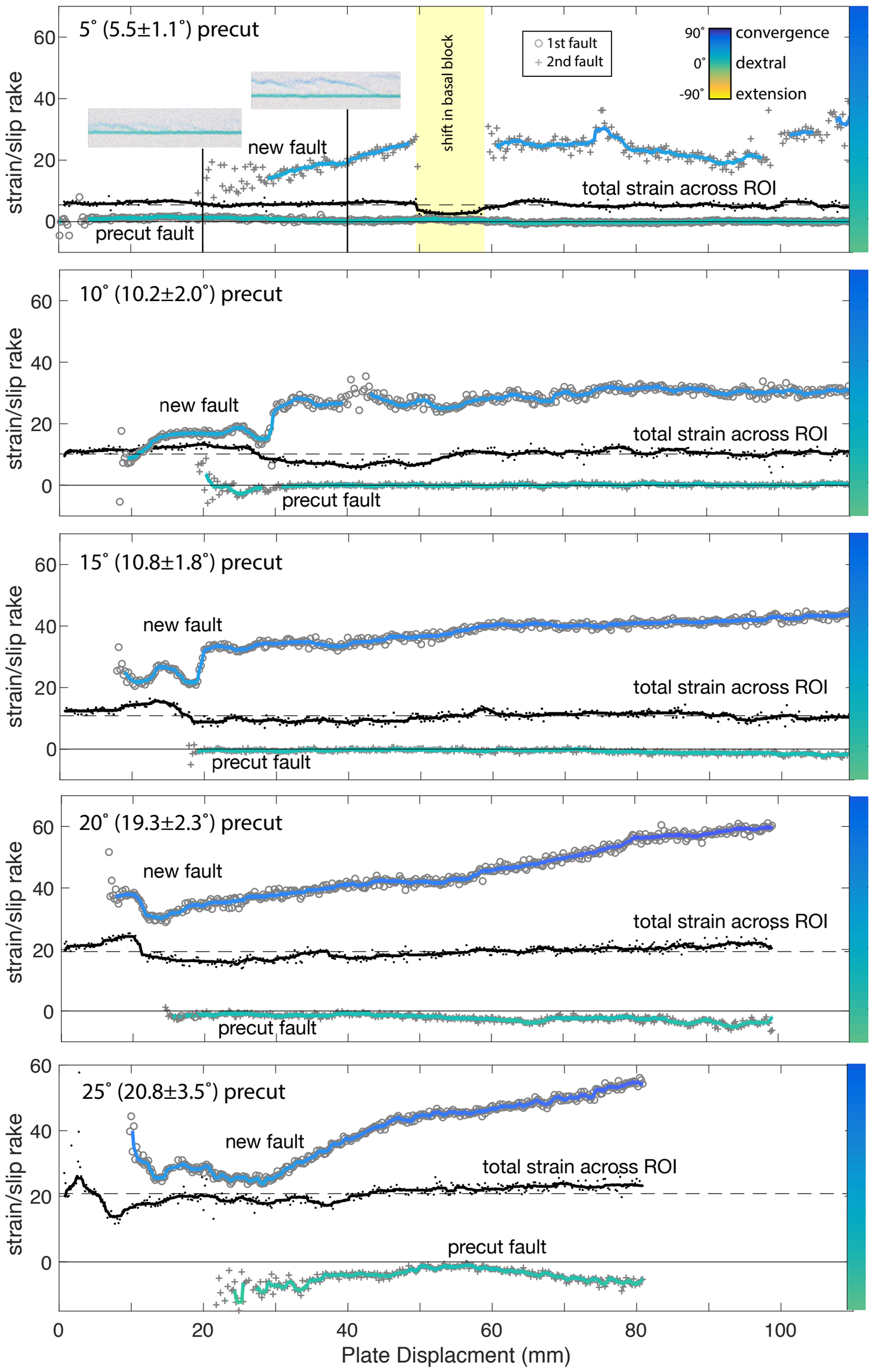

Figure 5: The experiments with precut vertical surface show two types of slip partitioning depending on convergence angle. Black lines (11-point median filter through data) show the convergence across the ROI of the experiment with mean convergence reported in parentheses next to the convergence angle input to the stepper motors. Colored lines (11-point median filter through data) show the evolution of slip sense for each experiment with both placement and hue of the line indicating slip sense. The slip sense on the faults evolves during the experiments as new faults develop. Within the 5˚ experiment, the precut surface has dextral slip prior to growth of the new thrust fault. Under larger convergence angles (10˚-25˚; B-E) the thrust fault forms prior to dextral slip along the precut surface.

292 experiments both reactivate later in the experiment (Figure 5). The details of the temporally
293 variable slip rates along faults in these experiments is beyond the scope of this paper.
294 The moderate convergence experiments develop several (1-3) small extensional features that
295 strike oblique to the precut faults. These features develop adjacent to the dextral fault within the
296 sliver between this fault and the reverse fault. For example, the 15˚ convergence experiment
297 develops an extensional crack oriented 20˚ clockwise from the dextral fault at around 80 mm
298 plate displacement (Figure 5). The crack in the 15˚ experiment, as well as those of other
299 moderate convergence precut experiments, opens too slowly for the incremental dilatational
300 strain associated with opening to be distinguished out of the noise of the DIC.

301 ***4.1.1 Fault geometry in precut experiments***

302 We can estimate the geometry of the faults by presuming that all faults extend linearly from
303 the surface trace to the position of the basal dislocation. To confirm this assumption, we created
304 trenches across the faults at the end of each experiment and examined a few of trenches from the
305 precut fault in detail (Figure 6). Although the homogeneously colored kaolin doesn't
306 immediately reveal faults in cross-section, further displacement of the basal blocks produces
307 visible offset of the trench wall along the active faults. These trenches confirm that both strike-
308 slip and reverse faults root at the block edge discontinuity (Figure 6). Additionally, the dip of
309 faults in the clay generally remain constant with depth (Figure 6).
310 Due to the scalloped nature of the reverse faults, the dips of these faults vary spatially across
311 the experiments as well as temporally though the evolution of the system. The minimum dip
312 values are constrained by the fault scarp positioned farthest from the block edge and the
313 maximum dip approaches vertical where active reverse faults intersect the precut fault. Table 2
314 presents the range of active reverse fault dips calculated from the distance between the reverse

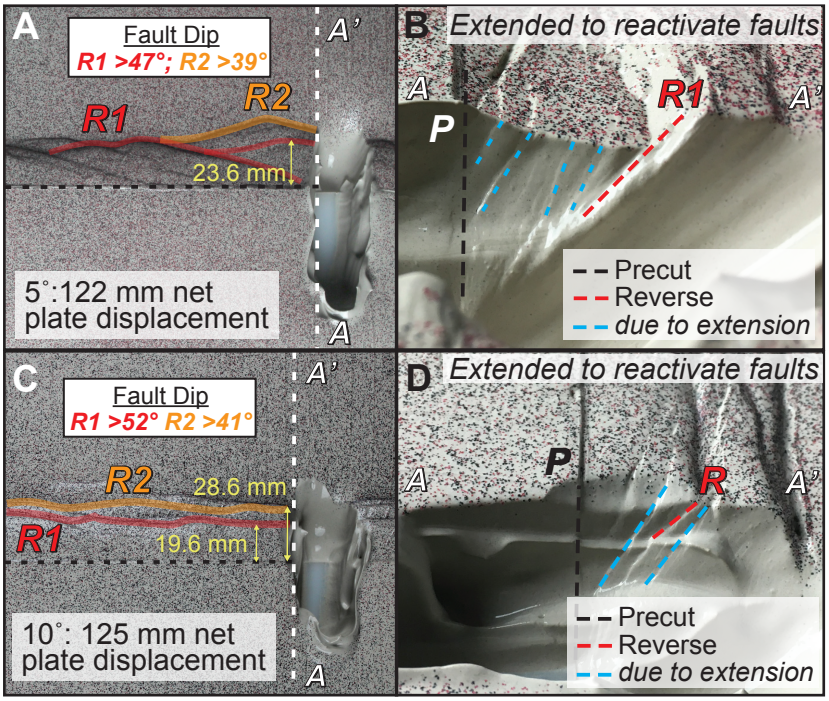

Figure 6: Example trenches excavated at the end of the 5˚ and 10˚ convergence precut experiments. A) & C) Map view with first, R1, and second, R2, reverse faults for 5˚ and 10˚ precut experiments respectively. B) & D) Cross-section view of trench wall in A) and C) respectively, after extension to re-activate reverse faults. Trench wall offsets reveal fault dip, which is constant with depth. Some new faults form during extension (blue dashed).

Table 2: Active reverse fault dips in precut experiments

	Onset of slip partitioning		2nd generation reverse faults	
Experiment	Net plate displacement	Reverse fault dip	Net plate displacement	Reverse fault dip
5˚P	48 mm	47˚-68˚	110 mm	42˚-54˚
10˚P	26 mm	50˚-58˚	85 mm	41˚-48˚
15˚P	20 mm	45˚-56˚	75 mm	34˚-46˚
20˚P	20 mm	42˚-52˚	72 mm	34˚-44˚
25˚P	30 mm	43˚-51˚	81 mm	32˚-44˚

fault trace and the pre-cut surface both at the onset of slip partitioning and later in the experiment. The second generation of reverse faults have shallower dip than the first generation (Table 2). Interestingly, none of the reverse faults dips as shallowly as the basal discontinuity, which dips 30˚. The increase of fault dip with decreasing convergence is consistent with oblique convergence experiments of dry sand (e.g., Burbidge and Braun, 1998; Leever et al., 2011).

4.1.2 Slip sense evolution along faults in precut experiments

To assess the overall sense of each fault throughout the experiments, we calculate the median incremental vorticity and divergence along the fault zone and use Equation 2 to find the slip sense. For all precut experiments, the simultaneous occurrence of reverse-slip on one fault and strike-slip on another signals the development of slip partitioning (Figure 5). Within all precut experiments, once slip partitioning starts, the slip rakes on the reverse and strike-slip faults diverge from each other; the reverse faults accommodate greater contraction, and the strike-slip faults accommodate nearly pure dextral slip, with some extension. This suggests that slip partitioned systems are more stable than oblique-slip faults under oblique convergence.

Within the experiment with the lowest tested convergence angle (5°), the mean slip rake along the precut fault remains very close to purely strike-slip. This is lesser convergence than applied to the system, suggesting that convergent strain is accommodated off of the fault. Just after 20 mm net plate displacement a set of new echelon faults develop with oblique- and mostly strike-slip rake (rake < 20˚ Figure 5). With greater plate displacement, these faults link and accommodate greater degree of contraction reaching steady-state slip rake of ~20˚. This reverse fault ceases activity from about 50-60 mm of plate displacement corresponding to a shift in the basal block that temporarily decreased the convergence angle. When the wedge re-stabilized to 5˚ convergence, the reverse fault resumed slip.

For precut experiments with convergence angles of 10° to 25°, reverse faults form first and the precut surfaces do not show dextral slip until after the reverse faults are established (Figures 4 and 5). Prior to slip partitioning the reverse faults have oblique-slip that is initially greater than the applied convergence angle (Figure 5). This suggests that dextral strain is accommodated off of these faults. After the onset of slip partitioning, the reverse faults accommodate greater contraction as the fault system evolves (Figure 5). The higher convergence angle experiments produce higher slip rakes on the reverse faults (greater contraction). While the reverse faults accommodate increased contraction with slip partitioning, the precut surface that start with purely dextral slip accommodate increasing degree of extension later in the experiments. Interestingly, higher convergence angles result in greater extension on the strike-slip fault (Figure 5).

4.2 Uncut experiments

The uncut experiments show three different styles of slip partitioning. The shallow convergence experiment (5˚ convergence) grows a sub-vertical dextral slip fault early in the experiment and later develops slip partitioning along almost the entire margin with the development of dipping reverse faults (Figure 7). This evolution is similar to that of the 5˚ precut experiment except that in the uncut experiment, the dextral fault coalesces from a series of echelon segments. The linkage of the echelon segments resembles that of pure strike-slip experiments (e.g., Hatem et al., 2017), and the resulting irregular geometry strongly controls the pattern of slip rake on the dextral fault (Figure 7).

The other two styles of slip partitioning arise in the moderate convergence angle (>5˚ convergence) uncut experiments that all first grow dipping reverse faults. The uncut experiments with convergences angles of 10˚-25˚ all develop local slip partitioning where two generations of

This figure is an animation click to start

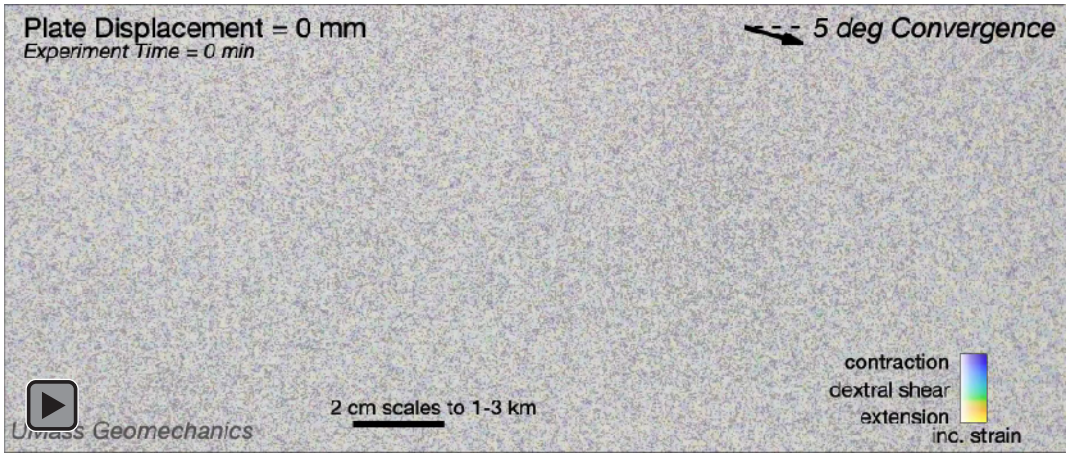

Figure 7: Animation of strain overlain on photos of the 5˚ convergence uncut experiment. Hue corresponds to sense of strain and saturation reveals strain rate. For clarity the animation shows only part of the total ROI.

This figure is an animation click to start

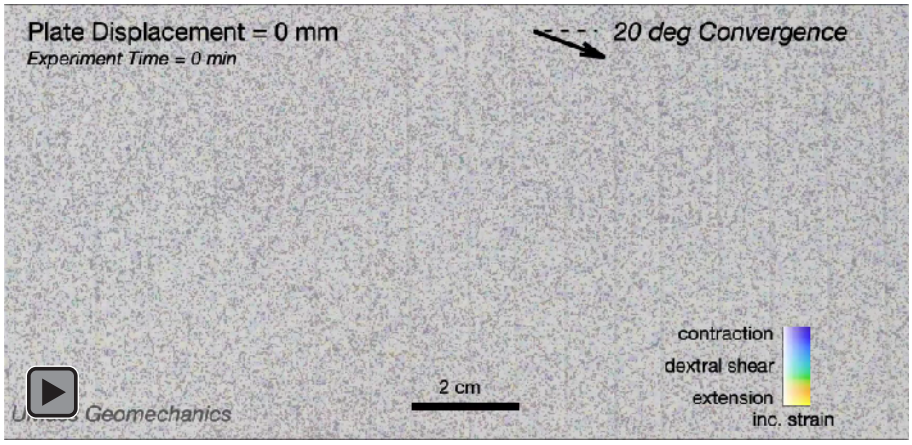

Figure 8: Animation of strain overlain on photos of the 20˚ convergence uncut experiment. Hue corresponds to sense of strain and saturation reveals strain rate. For clarity the animation shows only part of the total ROI.

dipping faults are simultaneously active. In this region of the experiment, the outboard more shallowly dipping fault accommodates greater convergence and the inboard steeper fault accommodates greater strike slip (Figure 8, 30-70 mm plate displacement). This style of slip partitioning is limited to the region of the experiment where the two generations of faults are both active, which varies throughout the evolution of the system. Outside of the region of local slip partitioning, deformation is accommodated as oblique slip along a single reverse fault and the earlier generation is abandoned when the second generation of reverse faults develops.

The third style of slip partitioning involves development of a new strike-slip fault after significant accumulation of reverse slip along the reverse faults in the 20˚ and 25˚ uncut experiments (Figure 8, >70 mm plate displacement). This slip partitioning style, which extends along the entire experiment, resembles the slip partitioning style of the precut experiments with moderate convergence angle, except that the new strike-slip fault grows by coalescence of initially dilatational echelon cracks and develops much later in the experiment. The irregular geometry of this new dextral fault, and corresponding variations in slip rake, owe to the linkage of the echelon cracks.

4.2.2 Fault geometry in uncut experiments

Fault trenches made at the end of the 5˚-20˚ uncut experiment confirm the location of the basal dislocation and fault geometry. The position of the reverse fault traces relative to the basal dislocation shows that the overall dip of the reverse faults in the higher convergence experiments is shallower than dips of reverse faults within the lower convergence experiments (Figure 9). These findings are consistent with those of the precut experiments (Table 2). Within the 5° uncut experiment, different echelon strands of the strike-slip fault form with dips ranging from 67˚ to

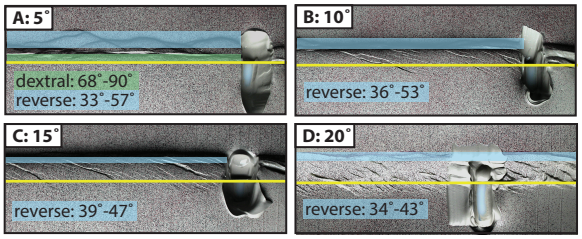

Figure 9: Map view of trenches for uncut experiments with convergence of 5˚ to 20˚. We use distance from the fault trace to the basal block edge revealed within the trench to estimate fault dips. Shaded areas show extent of reverse (blue) and dextral (green) faults. The new strike-slip fault in the 20˚ convergence experiment develops over the basal discontinuity. Smooth region in D indicates where clay was removed for sampling prior to the photo.

384 90˚. The reverse fault dips at the end of the uncut experiments (Figure 9) are similar to the dips
385 of the second generation of reverse fault dips within the precut experiments (Table 2).
386 Within the 10˚ convergence experiment, echelon opening cracks oriented 15-20˚ clockwise
387 from the basal discontinuity (at the end of the experiment) develop in the hanging wall of the
388 reverse faults, primarily between the reverse fault and the basal discontinuity (Figure 9B).
389 Within the 15˚ convergence these opening cracks are oriented in 20-25˚ clockwise from the basal
390 discontinuity at the end of the experiment (Figure 9C). At the end of the 20˚ convergence
391 experiment the echelon cracks are oriented 20˚-35˚ from the basal discontinuity and have linked
392 up to from a new strike-slip fault with irregular trace (Figure 9D). The animation of Figure 8
393 shows that the echelon cracks rotate significantly during linkage and evolution to a dextral fault.
394 The new strike-slip fault within the 20˚ convergence experiment develops over the basal
395 discontinuity.

396 ***4.2.3 Slip sense evolution along faults in uncut experiments***

397 Within all uncut experiments, the simultaneous slip on two parallel faults with different slip
398 sense indicates the development of slip partitioning (Figure 10). The onset of both local and
399 global slip partitioning is later in the uncut experiments than the experiments with an existing
400 vertical weakness (Figures 5 and 10). Furthermore, the onset of slip partitioning is earlier within
401 the higher convergence experiments. Whether the slip partitioning is local or global, after a
402 second fault develops, the slip sense on the two faults diverge from one another; the steeper fault
403 accommodates greater dextral slip while the more shallowly dipping fault accommodates greater
404 convergence.
405 Local slip partitioning in the 10˚, 15˚, and 20˚ uncut experiments generally develops earlier
406 for higher convergence angles (Figure 10). This is consistent with greater convergence

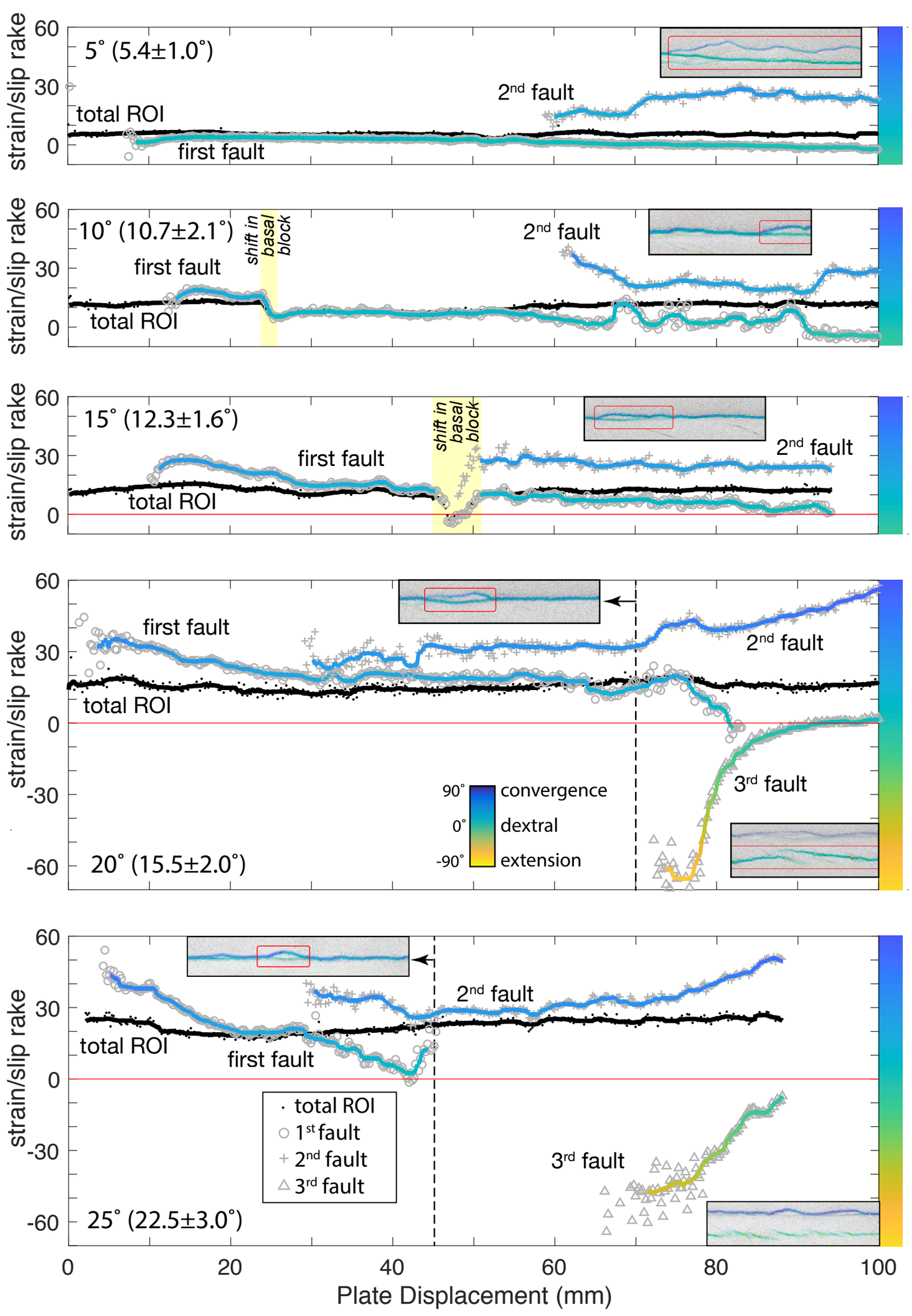

Figure 10: The uncut experiments show three different types of slip partitioning depending on convergence angle. Black lines and colored lines are as in Figure 3. The slip sense on the faults evolves during the experiments as new faults develop resulting in either slip partitioning along the entire margin (5˚, 20˚ & 25˚) or local slip partitioning (>5˚). For local slip partitioning, the early reverse fault converts to strike-slip when a new outboard reverse fault develops. For strain partitioning along the entire margin, the order depends on convergence angle. Whereas the 5˚ experiment grows a strike-slip fault and then a new thrust fault, the 20˚ and 25˚ experiments grow a thrust fault and later a strike-slip fault.

facilitating the development of the second generation of reverse faults that starts local slip partitioning. The local slip partitioning results in slip rakes on the two faults that differ by ~25˚ (Figure 10). The marked decrease in convergence angle from 45-52 mm plate displacement for the 15° experiment owes to an episode of slight tilting (back rotation) of the center block beneath the clay. During this period of basal block tilting, the previously oblique-convergence slipping fault accommodates oblique-normal slip. In this experiment, slip partitioning initiated immediately following the block rotation and associated extension.

Global slip partitioning in the 20˚ and 25˚ uncut experiments occurs when initially dilatational echelon cracks link and accommodate greater dextral slip (Figure 10). While the slip sense along the new coalescing fault evolves, the reverse fault accommodates greater contraction than achieved within any of the experiments with local patches of slip partitioning. The local slip partitioning in the uncut experiments has lesser difference between slip rakes on the two faults then either the of the global slip partitioning styles for the uncut experiments or the global partitioning of the precut experiments (Figures 5 & 10). Because both faults of the local slip partitioning dip, they are both able to accommodate convergence. This differs from the other two styles of slip partitioning where the (sub-)vertical fault cannot effectively accommodate convergence so that slip rake differ more substantially between the two slip partitioned faults.

5 DISCUSSION

Whether or not the experiments have a pre-existing vertical weakness, slip partitioning develops in all experiments as one of three different styles. Two of the styles resulting in persistent slip partitioning along the entire margin of the experiment while the third style of local slip partitioning is transient. Experiments with low convergence angle of 5° initially develop a strike-slip fault — either along the precut vertical surface or as a newly grown sub-vertical fault

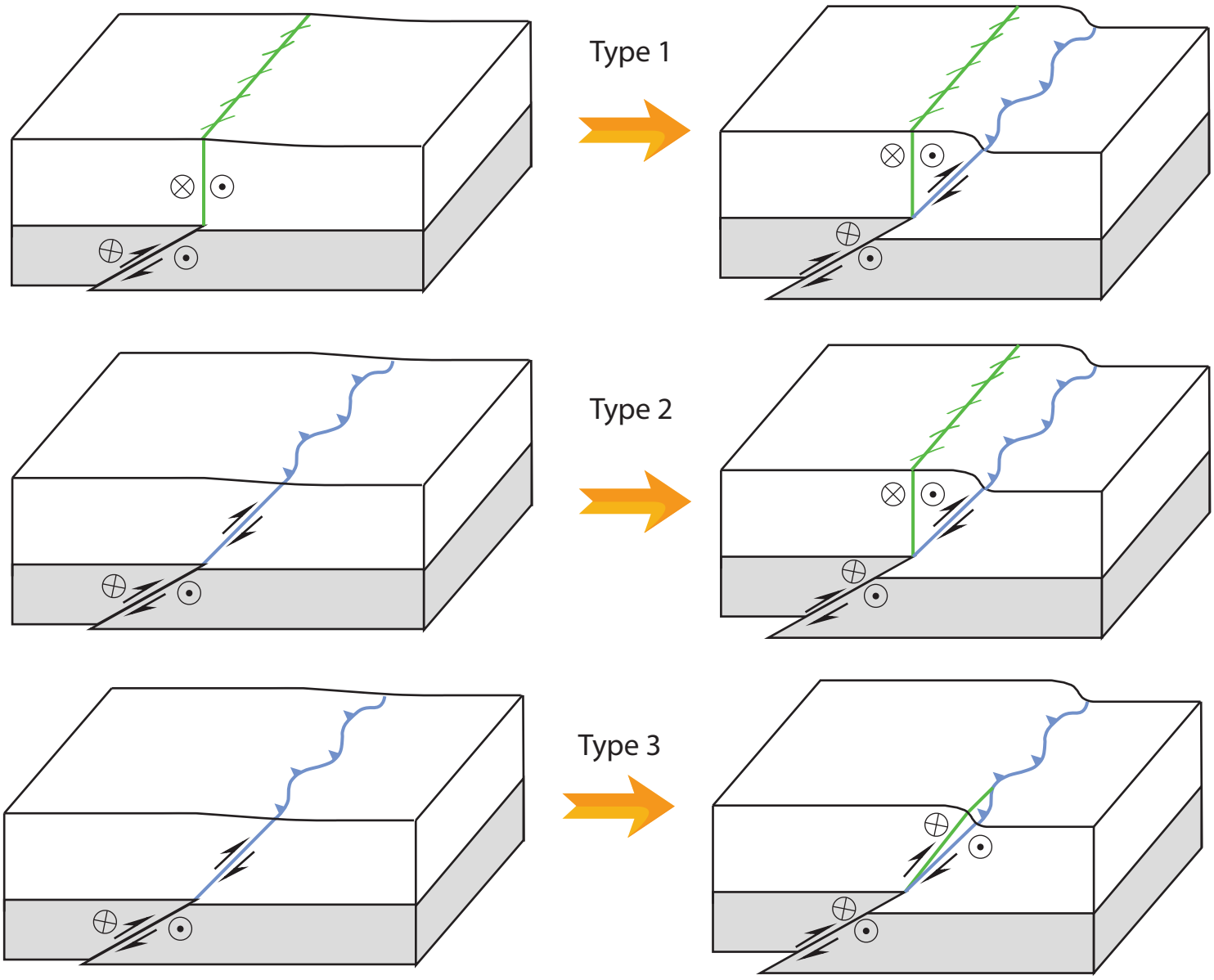

Figure 11: Three styles of slip partitioning. Top row: Global slip partitioning develops in low convergence experiments with the development of a reverse slip fault after the initial dextral slip fault. Middle row: In moderate convergence experiments, global slip partitioning develops with the grow of a dextral fault after the initiation of the reverse fault. Bottom row: Local slip partitioning develops when a new more shallowly dipping reverse fault grows while the older fault remains active. This style of local slip partitioning may be short-lived.

in the uncut experiment. In this first style of slip partitioning, the formation of the reverse fault marks the start of slip partitioning along the entire margin (Figure 11 top row).

Higher convergence angle experiments (10°, 15°, 20° & 25˚) demonstrate the second and third styles of slip partitioning. The second style of global slip partitioning evolution arises in the precut experiments with convergence > 5˚ and in the uncut experiments with > 15˚ convergence. In the precut experiments, the vertical weakness does not slip first due to the clamping effect of the convergence. Instead, a new oblique-slip reverse fault forms (Figure 11 middle row). Once convergent strain is accommodated along the reverse fault, the precut fault begins to slip in strike-slip. This pattern of fault development is well illustrated in the 15° precut experiment (Figure 4). The second style of slip partitioning also develops in some of the higher convergence uncut experiments. Late in the experiments, the 20˚ and 25˚ uncut experiments grow a new strike-slip fault that produces global slip partitioning (Figures 8 & 11). Although the 10˚ and 15˚ uncut experiments did not develop a new strike-slip fault, dilatational cracks formed within the hanging wall of the reverse faults. If the experiments had continued longer, these cracks may have coalesced to form a through-going dextral fault.

The uncut experiments with 10°, 15°, 20˚ and 25° convergence angles also show a third style of local slip partitioning development. Similarly to the precut experiments under these same convergences, an oblique-reverse fault first forms in the uncut experiments (Figure 11). The development of a second generation of reverse faulting outboard of the first, can produce local slip partitioning if both faults remain simultaneously active (Figure 11 bottom row). Where this happens, the newer reverse fault accommodates greater contraction than the steeper dipping fault, resulting in local slip partitioning. This third style of slip partitioning is spatially limited and can be short-lived as the older fault segment becomes abandoned.

5.2 Mechanisms for the development of slip partitioning

The development of two parallel striking faults that partition slip rather than a single oblique-slip fault may owe to both the geometry of the first fault to form and to asymmetry of the strain field associated with oblique slip. Under low convergence, i.e. 5˚ convergence tested here, the first fault forms a steeply dipping strike-slip fault. Because this steep fault cannot efficiently accommodate convergence, further deformation of the system leads to accumulation of off-fault contraction (Figure 12A). The contraction on the driving block side of the strike-slip fault promotes the development of a dipping reverse fault that marks the onset of slip partitioning. Under moderate convergence, 10˚-25˚ tested here, the first fault to form is a dipping oblique-slip fault with scalloped trace. The along strike roughness of the fault may limit the degree of strike-slip that the fault can accommodate as the strike-slip is impeded around large asperities. Because the slip on these faults accommodates greater convergence than the overall convergence applied to the system (Figures 5 & 10), off-fault shear strain accumulates around the fault (Figure 12B). This distributed off-fault shear strain can promote either slip along an existing steeper surface or the development of a new strike-slip fault.

The DIC from the experiments of this study reveal that asymmetry of the strain field around early reverse faults also contributes to the development of strike-slip faults. Dilation along a transect across the ROI within the 15˚ uncut experiment shows a region of extension within the hanging wall of the reverse fault (Figure 12 C). The development of both new dextral faults and dextral slip along existing surfaces occurs within the region of extension in the hanging wall of the reverse fault. Considering that the overall loading of the system is oblique convergence, the development of local extensional strain, while not unexpected, is nevertheless remarkable. The local extension could arise from a combination of flexure of the clay and/or unclamping by

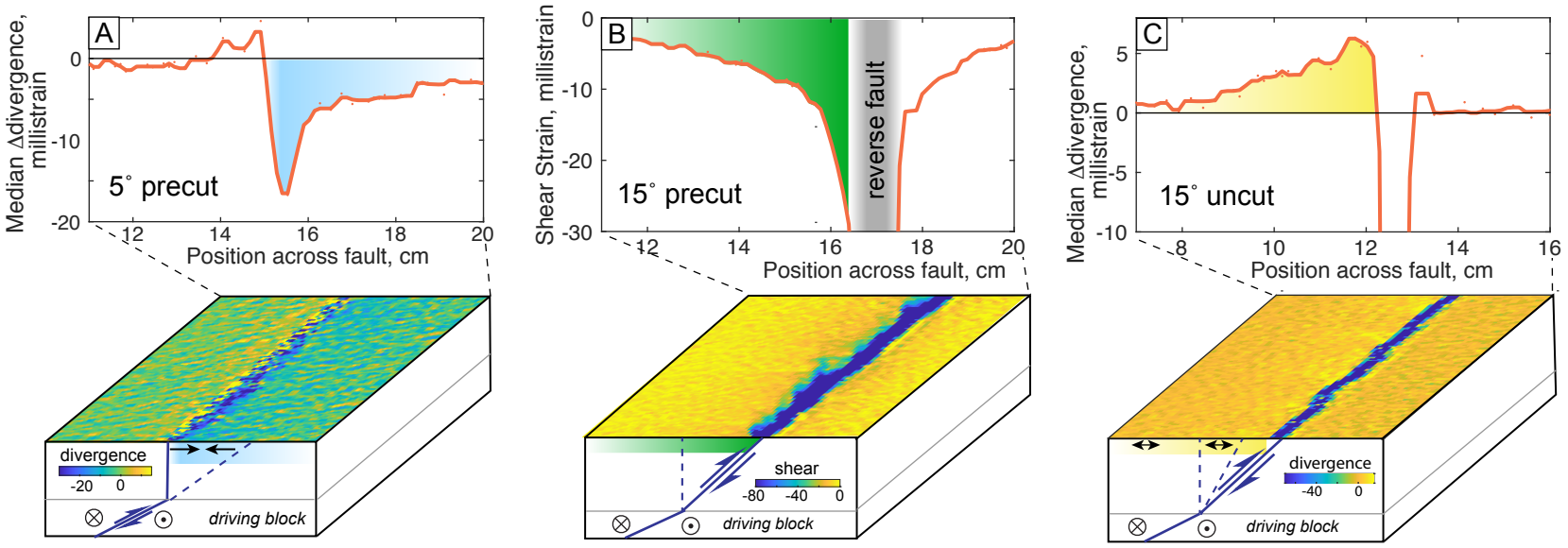

Figure 12: Top row median strain across the strain maps shown on sketch blocks in bottom row. Plots show strain along a transect perpendicular to faults. A) Divergence within the 5˚ precut experiment from 14-16 m plate displacement prior to the growth of the reverse fault. Sketch shows the development of off-fault convergence on the driving block side of the dextral fault that promotes reverse fault development. B) Shear strain within the 15˚ precut experiment from 14-16 mm of plate displacement prior to the growth of the dextral fault. Off-fault shear strain indicates inefficient accommodation of strike-slip. Sketch of off-fault shear strain that promotes growth of the strike slip fault in the hanging wall of the reverse fault. C) Divergence of the displacement field shows extension and unclamping within the hanging wall of the first thrust fault. Median divergence from 24 - 26 mm plate displacement plotted for uncut experiments with 15˚ convergence angle (prior to dextral slip). Sketch shows the development of extension in the hanging wall of the reverse fault that unclamps any existing faults (e.g., dashed).

476 reverse fault slip. Shallow extension near the upper surface of the clay may develop from flexure
477 of the hanging wall associated warping of the clay over the basal discontinuity (Figure S1).
478 Flexural stresses are only expected to be tensile above the neutral surface and may not account
479 for dextral faulting observed at depth (Figure 6). Furthermore, the change in fault dip from the
480 30˚ basal discontinuity to the steeper reverse fault would enhance contraction at depth. In
481 contrast, dip slip along the reverse fault may unclamp the full depth of existing surfaces in the
482 hanging-wall and promote slip. Such unclamping of strike-slip faults via reverse fault slip has
483 been proposed within crustal slip partitioned fault systems (e.g., ten Brink and Lin, 2004).
484 Within the experiments of this study, some combination of warping and unclamping can account
485 for why the vertical precut surfaces in the > 5˚ convergence experiments do not slip until after
486 accumulation of reverse-slip along the more shallowly dipping faults. These mechanisms also
487 account for the observation that higher convergence angle experiments produce greater local
488 dilation on the dextral faults (Figures 5 & 10); the greater reverse slip in the higher convergence
489 experiments increases the local hanging-wall extension.

490 ***5.2 Comparison to oblique convergence experiments in dry sand***

491 The wet kaolin experiments here show many similar features of fault evolution under oblique
492 convergence as experiments in dry sand. Pairs of slip partitioned faults in both sand and wet
493 kaolin have slip sense that diverge from one another after the onset of slip partitioning (Figures 5
494 & 10; Leever et al., 2011). As faults remain active, the reverse fault accommodates greater
495 convergence and the sub-vertical fault accommodates greater strike-slip. This behavior suggests
496 that slip partitioned fault systems become more stable as they evolve, and slip-partitioned fault
497 systems are not likely to evolve towards a single fault with oblique slip. The stability of fault slip
498 partitioning in experiments with very different rheology (i.e., dry sand and wet kaolin) and

boundary conditions suggests that the development and persistence of slip partitioning relies on fault geometry rather than rheologic properties.

The wet kaolin experiments here show that the presence of a precut surface and higher convergence angles generally lead to slip partitioning at lower total accumulated strain. These results support the conclusions of previous experiments (Chemenda et al., 2000; McClay et al., 2004; Haq and Davis, 2010; Leever et al., 2011) that the evolution of a slip-partitioned fault system is controlled both by the angle of convergence and pre-existing weaknesses. In particular, the earlier onset of slip partitioning when the vertical weakness is precut in the wet kaolin support conclusions by Chemenda et al. (2000) as well as Haq and Davis (2010) that pre-existing weak zones foster slip partitioning.

The experiments in wet kaolin develop slip partitioning within stages similar to those proposed by Leever et al. (2011) and also documented by McClay et al., (2004) in dry sand: (1) early strain accumulation, (2) separate formation of reverse and strike-slip faults, and (3) active slip along both reverse and strike-slip faults. The wet kaolin experiments with moderate convergence angle resemble experiments in dry sand that develop an early reverse fault before slipping along a strike-slip fault; however low convergence angle (5˚ tested here) produce strike-slip faults prior to reverse faults. The latter behavior is not observed in dry sand oblique convergence experiments. Leever et al. (2011) observed early echelon cracks under low convergence (4˚), but these cracks did not link to form a strike-slip fault until after two reverse faults formed in their experiments. Furthermore, across all of the tested convergence angles, slip partitioning within dry sand experiments develops under less total applied strain for similar convergence angle than in wet kaolin. Dry sand is not able to compact as much as wet kaolin; upon compaction, sand forms force chains before localizing reverse faults (e.g., Rechenmacher et

al., 2010). Consequently, dry sand readily forms reverse faults early in the oblique convergence experiments, even under low convergence angles. In concert with accommodating distributed compaction before localized faulting, the wet kaolin has non-zero cohesion, which delays the onset of faulting and promotes long-lived activity along existing faults. The utilization of existing weaknesses in the wet kaolin experiments for both slip along precut surfaces and for local slip partitioning, rather than growing new faults, is also consistent with the non-zero cohesion of wet kaolin. Despite the rheologic differences between dry sand and wet kaolin, both materials develop persistent slip partitioning along the entire margin, suggesting that this behavior should be expected in a wide range of crustal materials.

5.3 Implications for development of slip partitioning in the crust

Slip partitioning may initiate either at transform or convergent plate boundaries that begin to accommodate oblique convergence. For example, the Haida Gwaii portion of the Queen Charlotte transform fault in Canada accommodates slight convergence along young reverse faults within this part of the transform fault system (e.g., Lay et al., 2013; Rohr, 2015; Brothers et al., 2018; ten Brink et al., 2018). The low convergence angle experiments of this study suggest that even with the introduction of convergence, transform faults can remain active because the reverse slip on the new contractional fault system unclamps the transform fault, thereby facilitating slip. Consequently, we might expect slip partitioned fault systems to persist as long as the oblique convergent loading, general fault configuration, and fault strength do not change.

Convergent margins may develop slip partitioning as they either develop new strike-slip faults or reactivate existing weaknesses in strike-slip. Reactivation of existing weaknesses may facilitate the development of slip partitioning at higher convergence angles than otherwise permitted (e.g., Chemenda et al., 2000; Haq and Davis, 2010). Slip partitioning at margins with

high convergence angles may also be facilitated by magmatic weakening of the over-riding plate. Weakening of the crust through magmatic intrusion may localize strain that initiates large through-going strike-slip faults and facilitates slip partitioning (De Saint Blanquat et al., 1998). The findings from the scaled experiments of this study demonstrate that the presence of a weakness can facilitate slip partitioning at lower total strain than a more homogenous strength experiment.

While magmatic weakening may facilitate strike-slip faulting, the initiation of strike-slip faults within convergent margins may also facilitate magmatism. The scaled experiments of this study show the initiation of strike-slip faults via coalescence of opening cracks that strike oblique to the margin. These segmented opening-mode cracks have similar geometric relationships with the convergent margin as volcanic fissures in the southern Andes of Chile (e.g., Lara et al., 2006; Cembrano and Lara, 2009). These fissures that provide pathways for magma migration may thermally weaken the crust and promote the development of strike-slip faults. Furthermore, the slip partitioned nature of the of the oblique convergent fault system means that reverse faulting invokes extension in the hanging wall, which promotes development of volcanic fissures. Volcanism increased in some fissures after the 1960 Chile earthquake due to temporal changes in the local stress field (Lara et al., 2004). Consequently, magmatism in oblique convergent margins can lead to a positive feedback loop – where convergence enhances magmatism that weakens the crust, enabling strike-slip fault development that provides conduits for magmatism (De Saint Blanquat et al., 1998). One result of this feedback can be sustained slip partitioning of fault systems within oblique convergent margins.

6 CONCLUSIONS

The scaled experiments of oblique convergence over a basal dislocation exhibit slip partitioning along the entire margin that resembles slip partitioned crustal systems regardless of whether the experiments have a precut vertical weakness or not. The experiments reveal three styles of slip partitioning evolution delineated by the order of faulting and extent of slip partitioning. The first style observed in the low convergent angle experiments (5°) grows strike-slip faults prior to reverse faulting along the entire oblique convergent margin. The second style develops in all precut experiments with >5˚ convergence and uncut experiments with >15˚ convergence. In these experiments, the primarily reverse fault forms first and slip partitioning of the entire convergent margin develops with the development of strike slip either, along the precut fault or as a new fault. The uncut experiments also show a third style of local slip partitioning, where two generations of reverse faults are simultaneously active for a period of time in part of the experiment.

Scaled oblique convergence experiments in wet kaolin that simulate crustal materials develop a slip-partitioned fault system rather than developing a single oblique-slip active fault structure in order to accommodate oblique convergence. The development of two active fault surfaces, which consume greater work, arises due to the changes in the local stress state after development of the first fault. In systems that grow an early steeply dipping strike-slip faults, off-fault contraction accumulates until a new reverse fault grows. In systems that grow early reverse faults, the lobate nature of these faults limits accommodation of strike-slip, which increases distributed shear strain. Furthermore, reverse slip on the fault produces local extension in its hanging wall. Both of these mechanisms promote development of new strike-slip faults in the hanging wall of the reverse fault.

589 The emergence of fault slip partitioning within the scaled experiments, provides insight into
590 the development of such fault systems at crustal margins. Transform margins that begin to
591 accommodate convergence may develop a system of reverse faults, and convergent margins that
592 begin to accommodate oblique plate motion may develop new strike-slip faults or activate
593 inboard crustal weakness to accommodate strike-slip. Once the fault system is slip partitioned
594 along a substantial portion of the oblique convergent margin, this active fault configuration will
595 persist. The observation of slip partitioning under a wide range of experimental conditions in this
596 study of cohesive material, as well as in previous experiments within non-cohesive material,
597 demonstrates how such systems are frequently observed at oblique-convergent margins with a
598 variety of crustal materials around the world.

599 **7. DATA MANAGEMENT**

600 The experimental photographs are available on EPOS repository for analog modeling of geologic
601 processes hosted by GFZ Potsdam. Animations of strain and uplift are available on the UMass
602 Geomechanics YouTube channel transpression play list (https://tinyurl.com/y6fhkxeh).

603 **8. ACKNOWLEDGEMENTS**

604 This work was funded by NSF grant EAR 1550133. MLC thanks David Bowman and Karen
605 Leever for inspirational discussions on slip partitioned fault systems.

606 **9. REFERENCES**

607 Ackermann, R. V., Schlische, R.W., and Withjack, M.O., 2001, The geometric and statistical
608 evolution of normal fault systems: An experimental study of the effects of mechanical layer
609 thickness on scaling laws: Journal of Structural Geology, v. 23, p. 1803–1819,
610 doi:10.1016/S0191-8141(01)00028-1.

611 Bayarsayhan, C., Bayasgalan, A., Enhtuvshin, B., Hudnut, K.W., Kurushin, R.A., Molnar, P.,
612 and Olziybat, M., 1996, 1957 Gobi-Altay, Mongolia, earthquake as a prototype for southern

California's most devastating earthquake: Geology, v. 24, p. 579–582.

Bemis, S.P., Weldon, R.J., and Carver, G.A., 2015, Slip partitioning along a continuously curved fault: Quaternary geologic controls on Denali fault system slip partitioning, growth of the Alaska Range, and the tectonics of south-central Alaska: Lithosphere, v. 7, p. 235–246.

Bonanno, E., Bonini, L., Basili, R., Toscani, G., and Seno, S., 2017, How do horizontal, frictional discontinuities affect reverse fault-propagation folding? Journal of Structural Geology, v. 102, p. 147–167, doi:10.1016/j.jsg.2017.08.001.

Bonini, L., Basili, R., Toscani, G., Burrato, P., Seno, S., and Valensise, G., 2016, The effects of pre-existing discontinuities on the surface expression of normal faults: Insights from wet-clay analog modeling: Tectonophysics, v. 684, p. 157–175, doi:10.1016/j.tecto.2015.12.015.

Bowman, D., King, G., and Tapponnier, P., 2003, Partitioning by Elastoplastic Slip Propagation of Oblique Depth: Science, v. 300, p. 1121–1123, doi:10.1126/science.1082180.

Braun, J., and Beaumont, C., 1995, Three-dimensional numerical experiments of strain partitioning at oblique plate boundaries: Implications for contrasting tectonic styles in the southern Coast Ranges, California, and central South Island, New Zealand: Journal of Geophysical Research B: Solid Earth, v. 100, p. 18059–18074.

ten Brink, U., and Lin, J., 2004, Stress interaction between subduction earthquakes and forearc strike-slip faults: Modeling and application to the northern Caribbean plate boundary: Journal of Geophysical Research: Solid Earth, v. 109, p. 1–15, doi:10.1029/2004JB003031.

ten Brink, U.S., Miller, N.C., Andrews, B.D., Brothers, D.S., and Haeussler, P.J., 2018, Deformation of the Pacific/North America Plate Boundary at Queen Charlotte Fault: The Possible Role of Rheology: Journal of Geophysical Research: Solid Earth, v. 123, p. 4223–4242, doi:10.1002/2017JB014770.

Brothers, D.S., Andrews, B.D., Walton, M.A.L., Greene, H.G., Barrie, J.V., Miller, N.C., ten Brink, U., East, A.E., Haeussler, P.J., and Kluesner, J.W., 2018, Slope failure and mass transport processes along the Queen Charlotte Fault, southeastern Alaska: Geological Society, London, Special Publications, v. 477, p. SP477-30.

Burbidge, D.R., and Braun, J., 1998, Analogue models of obliquely convergent continental plate boundaries: Journal of Geophysical Research: Solid Earth, v. 103, p. 15221–15237, doi:10.1029/98jb00751.

Cembrano, J., and Lara, L., 2009, The link between volcanism and tectonics in the southern volcanic zone of the Chilean Andes: A review: Tectonophysics, v. 471, p. 96–113, doi:10.1016/j.tecto.2009.02.038.

Chemenda, A., Lallemand, S., and Bokun, A., 2000, Strain partitioning and interplate friction in oblique subduction zones: Constraints provided by experimental modeling: Journal of

Geophysical Research: Solid Earth, v. 105, p. 5567–5581, doi:10.1029/1999jb900332.

Clifton, A.E., Schlische, R.W., Withjack, M.O., and Ackermann, R. V., 2000, Influence of rift obliquity on fault-population systematics: Results of experimental clay models: Journal of Structural Geology, v. 22, p. 1491–1509, doi:10.1016/S0191-8141(00)00043-2.

Cooke, M.L., and Van Der Elst, N.J., 2012, Rheologic testing of wet kaolin reveals frictional and bi-viscous behavior typical of crustal materials: Geophysical Research Letters, v. 39, doi:10.1029/2011GL050186.

Cooke, M.L., Reber, J.E., and Haq, S.B., 2016, Physical Experiments of Tectonic Deformation and Processes : Building a Strong Community: GSA Today, v. 26, p. 36–37, doi:10.1111/j.1365-3121.

Cooke, M.L., Schottenfeld, M.T., and Buchanan, S.W., 2013, Evolution of fault efficiency at restraining bends within wet kaolin analog experiments: Journal of Structural Geology, v. 51, p. 180–192, doi:10.1016/j.jsg.2013.01.010.

DeGroot, D.J., and Lunne, T., 2007, Measurement of Remoulded Shear Strength: Norwegian Geotechnical Institute. Report, p. 20061021–20061023.

Dewey, J.F., and Lamb, S.H., 1992, Active tectonics of the Andes: Tectonophysics, v. 205, p. 79–95.

Eberhart-Phillips, D., Haeussler, P.J., Freymueller, J.T., Frankel, A.D., Rubin, C.M., Craw, P., Ratchkovski, N.A., Anderson, G., Carver, G.A., and Crone, A.J., 2003, The 2002 Denali fault earthquake, Alaska: A large magnitude, slip-partitioned event: Science, v. 300, p. 1113–1118.

Eisenstadt, G., and Sims, D., 2005, Evaluating sand and clay models: Do rheological differences matter? Journal of Structural Geology, v. 27, p. 1399–1412, doi:10.1016/j.jsg.2005.04.010.

Fitch, T.J., 1972, Plate convergence, transcurrent faults, and internal deformation adjacent to Southeast Asia and the western Pacific: Journal of Geophysical Research, v. 77, p. 4432–4460, doi:10.1029/JB077i023p04432.

Fitzgerald, P.G., Roeske, S.M., Benowitz, J.A., Riccio, S.J., Perry, S.E., and Armstrong, P.A., 2014, Alternating asymmetric topography of the Alaska range along the strike-slip Denali fault: Strain partitioning and lithospheric control across a terrane suture zone: Tectonics, v. 33, p. 1519–1533.

Gaudemer, Y., Tapponnier, P., Meyer, B., Peltzer, G., Shunmin, G., Zhitai, C., Huagung, D., and Cifuentes, I., 1995, Partitioning of crustal slip between linked, active faults in the eastern Qilian Shan, and evidence for a major seismic gap, the 'Tianzhu gap'', on the western Haiyuan Fault, Gansu (China)': Geophysical Journal International, v. 120, p. 599–645, doi:10.1111/j.1365-246X.1995.tb01842.x.

683 Gomez, F., Nemer, T., Tabet, C., Khawlie, M., Meghraoui, M., and Barazangi, M., 2007, Strain
684 partitioning of active transpression within the Lebanese restraining bend of the Dead Sea
685 Fault (Lebanon and SW Syria): Geological Society, London, Special Publications, v. 290, p.
686 285–303, doi:10.1144/290.10.

687 Haq, S.S.B., and Davis, D.M., 2009, Interpreting finite strain: Analysis of deformation in analog
688 models: Journal of Structural Geology, v. 31, p. 654–661, doi:10.1016/j.jsg.2009.03.017.

689 Haq, S.S.B., and Davis, D.M., 2010, Mechanics of fore-arc slivers: Insights from simple analog
690 models: Tectonics, v. 29, p. 1–14, doi:10.1029/2009TC002583.

691 Haq, S.S.B., and Davis, D.M., 1997, Oblique convergence and the lobate mountain belts of
692 western Pakistan: Geology, v. 25, p. 23–26.

693 Hatem, A.E., Cooke, M.L., and Madden, E.H., 2015, Evolving efficiency of restraining bends
694 within wet kaolin analog experiments: Journal of Geophysical Research: Solid Earth, v.
695 120, doi:10.1002/2014JB011735.

696 Hatem, A.E., Cooke, M.L., and Toeneboehn, K., 2017, Strain localization and evolving
697 kinematic efficiency of initiating strike-slip faults within wet kaolin experiments: Journal of
698 Structural Geology, v. 101, p. 96–108, doi:10.1016/j.jsg.2017.06.011.

699 Henza, A.A., Withjack, M.O., and Schlische, R.W., 2010, Normal-fault development during two
700 phases of non-coaxial extension: An experimental study: Journal of Structural Geology, v.
701 32, p. 1656–1667, doi:10.1016/j.jsg.2009.07.007.

702 Herbert, J.W., Cooke, M.L., Souloumiac, P., Madden, E.H., Mary, B.C.L., and Maillot, B., 2015,
703 The work of fault growth in laboratory sandbox experiments: Earth and Planetary Science
704 Letters, v. 432, doi:10.1016/j.epsl.2015.09.046.

705 Hubbert, M.K., 1937, Theory of scale models as applied to the study of geologic structures:
706 Geological Society of America Bulletin48, v. 48, p. 1459–1520.

707 Jones, C.H., and Wesnousky, S.G., 1992, Variations in Strength and Slip Rate Along the San
708 Andreas Fault System: Science, v. 256, p. 83–86.

709 King, G., Klinger, Y., Bowman, D., and Tapponnier, P., 2005, Slip-partitioned surface breaks for
710 the M w 7.8 2001 Kokoxili earthquake, China: Bulletin of the Seismological Society of
711 America, v. 95, p. 731–738.

712 Lara, L.E., Lavenu, A., Cembrano, J., and Rodríguez, C., 2006, Structural controls of volcanism
713 in transversal chains: Resheared faults and neotectonics in the Cordón Caulle-Puyehue area
714 (40.5°S), Southern Andes: Journal of Volcanology and Geothermal Research, v. 158, p. 70–
715 86, doi:10.1016/j.jvolgeores.2006.04.017.

716 Lara, L.E., Naranjo, J.A., and Moreno, H., 2004, Rhyodacitic fissure eruption in Southern Andes

(Cordón Caulle; 40.5°S) after the 1960 (Mw:9.5) Chilean earthquake: A structural interpretation: Journal of Volcanology and Geothermal Research, v. 138, p. 127–138, doi:10.1016/j.jvolgeores.2004.06.009.

Lay, T., Ye, L., Kanamori, H., Yamazaki, Y., Cheung, K.F., Kwong, K., and Koper, K.D., 2013, The October 28, 2012 Mw 7.8 Haida Gwaii underthrusting earthquake and tsunami: Slip partitioning along the Queen Charlotte fault transpressional plate boundary: Earth and Planetary Science Letters, v. 375, p. 57–70.

Leever, K.A., Gabrielsen, R.H., Sokoutis, D., and Willingshofer, E., 2011, The effect of convergence angle on the kinematic evolution of strain partitioning in transpressional brittle wedges: Insight from analog modeling and high-resolution digital image analysis: Tectonics, v. 30, doi:10.1029/2010TC002823.

Lockner, D., Byerlee, J.D., Kuksenko, V., Ponomarev, A., and Sidorin, A., 1991, Quasi-static fault growth and shear fracture energy in granite: Nature, v. 350, p. 39.

Loveless, J.P., and Meade, B.J., 2010, Geodetic imaging of plate motions, slip rates, and partitioning of deformation in Japan: Journal of Geophysical Research: Solid Earth, v. 115.

McCaffrey, R., 1992, Oblique plate convergence, slip vectors, and forearc deformation: Journal of Geophysical Research, v. 97, p. 8905–8915, doi:10.1029/92JB00483.

McCaffrey, R., 1996, Slip partitioning at convergent plate boundaries of SE Asia: Geological Society, London, Special Publications, v. 106, p. 3–18.

McClay, K.R., Whitehouse, P.S., Dooley, T., and Richards, M., 2004, 3D evolution of fold and thrust belts formed by oblique convergence: Marine and Petroleum Geology, v. 21, p. 857–877, doi:10.1016/j.marpetgeo.2004.03.009.

Michael, A.J., 1990, oblique motion has been explained by a kinematic model convergence required by the Pacific-North American this combination of motions is taken up by develop a simple physical on applying studies Hamilton ' s principle to the energy released in earthquakes: Geophysical Research Letters, v. 17, p. 1453–1456.

Norris, R.J., and Cooper, A.F., 2001, Late Quaternary slip rates and slip partitioning on the Alpine Fault, New Zealand: Journal of Structural Geology, v. 23, p. 507–520, doi:10.1016/S0191-8141(00)00122-X.

Oertel, G., 1965, The mechanics of faulting in clay experiments: Tectonophysics, v. 2, p. 343–393.

Platt, J.P., 1993, Mechanics of oblique convergence: Journal of Geophysical Research, v. 98, p. 16239, doi:10.1029/93jb00888.

Rechenmacher, A., Abedi, S., and Chupin, O., 2010, Evolution of force chains in shear bands in

sands: Geotechnique, v. 60, p. 343.

Richard, P., and Cobbold, P., 1990, Experimental insights into paritioning of fault motions in continental convergent wrench zones: Annales Tectonicae, v. 4, p. 35–44.

Rohr, K.M.M., 2015, Plate boundary adjustments of the southernmost Queen Charlotte fault: Bulletin of the Seismological Society of America, v. 105, p. 1076–1089.

De Saint Blanquat, M., Tikoff, B., Teyssier, C., and Vigneresse, J.L., 1998, Transpressional kinematics and magmatic arcs: Geological Society, London, Special Publications, v. 135, p. 327–340.

Schlische, R.W., Withjack, M.O., and Eisenstadt, G., 2002, An experimental study of the secondary deformation produced by oblique-slip normal faulting: AAPG bulletin, v. 86, p. 885–906.

Schreurs, G. et al., 2006, Analogue benchmarks of shortening and extension experiments: Geological Society, London, Special Publications, v. 253, p. 1–27, doi:10.1144/GSL.SP.2006.253.01.01.

Schreurs, G., Buiter, S.J.H., Boutelier, J., Burberry, C., Callot, J.-P., Cavozzi, C., Cerca, M., Chen, J.-H., Cristallini, E., and Cruden, A.R., 2016, Benchmarking analogue models of brittle thrust wedges: Journal of structural geology, v. 92, p. 116–139.

Schreurs, G., and Colletta, B., 1998, Analogue modelling of faulting in zones of continental transpression and transtension: Geological Society, London, Special Publications, v. 135, p. 59–79.

Tchalenko, J.S., 1970, Similarities between shear zones of different magnitudes: Geological Society of America Bulletin, v. 81, p. 1625–1640.

Thielicke, W., and Stamhuis, E., 2014, PIVlab–towards user-friendly, affordable and accurate digital particle image velocimetry in MATLAB: Journal of Open Research Software, v. 2.

Tikoff, B., and de Saint Blanquat, M., 1997, Transpressional shearing and strike-slip partitioning in the Late Cretaceous Sierra Nevada magmatic arc, California: Tectonics, v. 16, p. 442–459.

Toeneboehn, K., Cooke, M.L., Bemis, S.P., Fendick, A.M., and Rudolf, M., 2018, Stereovision Combined With Particle Tracking Velocimetry Reveals Advection and Uplift Within a Restraining Bend Simulating the Denali Fault: v. 6, p. 1–13, doi:10.3389/feart.2018.00152.

Upton, P., Koons, P.O., and Eberhart-Phillips, D., 2003, Extension and partitioning in an oblique subduction zone, New Zealand: Constraints from three-dimensional numerical modeling: Tectonics, v. 22, p. n/a-n/a, doi:10.1029/2002tc001431.

Vernant, P., and Chéry, J., 2006, Mechanical modelling of oblique convergence in the Zagros, Iran: Geophysical Journal International, v. 165, p. 991–1002.

Withjack, M.O., and Jamison, W.R., 1986, Deformation produced by oblique rifting: Tectonophysics, v. 126, p. 99–124.

Yu, G., Wesnousky, S.G., and Ekström, G., 1993, Slip partitioning along major convergent plate boundaries, *in* Shallow Subduction Zones: Seismicity, Mechanics and Seismic Potential Part 1, Springer, p. 183–210.

FIGURE CAPTIONS:

Figure 1: Example sketches of slip-partitioning at oblique convergent margins expressed as two active faults with parallel strike. The oblique subduction zone margin has reverse slip along the subduction zone and strike-slip along the inboard fault that hosts magmatic conduits (taken from Tikoff and de Saint Blanquat, 1997).

Figure 2: Schematic of model geometry depicting the three plastic blocks with abutting 30° contacts and 2.5 cm of overlying wet kaolin clay. The blocks are positioned by two metal plates: one fixed and the other driven obliquely (°, measured from margin parallel) by two 90° opposed stepper motors. (B) Two DSLR cameras mounted above the model capture high-resolution images of the region of interest (ROI) shown in the red-dashed box. To form precut surface, an electrified copper wire (24 AWG, ~0.5 mm) is stretched tight with a wooden bow (B) and used to cut a discrete vertical fault parallel to and directly above the dipping block contact before starting the motors.

Figure 3: Animation of strain overlain on photos of the 5˚ convergence precut experiment. Hue corresponds to sense of strain and saturation reveals strain rate. For clarity the animation shows only part of the total ROI.

Figure 4: Animation of strain overlain on photos of the 15˚ convergence precut experiment. Hue corresponds to sense of strain and saturation reveals strain rate. For clarity the animation shows only part of the total ROI.

Figure 5: The experiments with precut vertical surface show two types of slip partitioning depending on convergence angle. Black lines (11-point median filter through data) show the

convergence across the ROI of the experiment with mean convergence reported in parentheses next to the convergence angle input to the stepper motors. Colored lines (11-point median filter through data) show the evolution of slip sense for each experiment with both placement and hue of the line indicating slip sense. The slip sense on the faults evolves during the experiments as new faults develop. Within the 5˚ experiment, the precut surface has dextral slip prior to growth of the new thrust fault. Under larger convergence angles (10˚-25˚; B-E) the thrust fault forms prior to dextral slip along the precut surface.

Figure 6: Example trenches excavated at the end of the 5˚ and 10˚ convergence precut experiments. A) & C) Map view with first, R1, and second, R2, reverse faults for 5˚ and 10˚ precut experiments respectively. B) & D) Cross-section view of trench wall in A) and C) respectively, after extension to re-activate reverse faults. Trench wall offsets reveal fault dip, which is constant with depth. Some new faults form during extension (blue dashed).

Figure 7: Animation of strain overlain on photos of the 5˚ convergence uncut experiment. Hue corresponds to sense of strain and saturation reveals strain rate. For clarity the animation shows only part of the total ROI.

Figure 8: Animation of strain overlain on photos of the 20˚ convergence uncut experiment. Hue corresponds to sense of strain and saturation reveals strain rate. For clarity the animation shows only part of the total ROI.

Figure 9: Top row: Map view of trenches for uncut experiments with convergence of 5˚ to 20˚. E) Map view of a trench excavated at the end of the 5˚ uncut experiment with main structures identified. Note: cross-section not through point of minimum dip for SS1 or R1. F) Cross-section view of trench verifying dip of structures. Dip values in cross-section show reasonable agreement (±2°) with dip values calculated from estimated block edge location. (R1a, R1b) reveal a shallowing of the fault as it propagated from depth

Figure 10: The uncut experiments show three different types of slip partitioning depending on convergence angle. Black lines and colored lines are as in Figure 3. The slip sense on the faults evolves during the experiments as new faults develop resulting in either slip partitioning along the entire margin (5˚, 20˚ & 25˚) or local slip partitioning (>5˚). For local slip partitioning, the early reverse fault converts to strike-slip when a new outboard reverse fault develops. For slip partitioning along the entire margin, the order depends on

convergence angle. Whereas the 5˚ experiment grows a strike-slip fault and then a new thrust fault, the 20˚ and 25˚ experiments grow a thrust fault and later a strike-slip fault.

Figure 11: Three styles of slip partitioning. Top row: Global slip partitioning develops in low convergence experiments with the development of a reverse slip fault after the initial dextral slip fault. Middle row: In moderate convergence experiments, global slip partitioning develops with the grow of a dextral fault after the initiation of the reverse fault. Bottom row: Local slip partitioning develops when a new more shallowly dipping reverse fault grows while the older fault remains active. This style of local slip partitioning may be short-lived.

Figure 12: Top row median strain across the strain maps shown on sketch blocks in bottom row. Plots show strain along a transect perpendicular to faults. A) Divergence within the 5˚ precut experiment from 14-16 m plate displacement prior to the growth of the reverse fault. Sketch shows the development of off-fault convergence on the driving block side of the dextral fault that promotes reverse fault development. B) Shear strain within the 15˚ precut experiment from 14-16 mm of plate displacement prior to the growth of the dextral fault. Off-fault shear strain indicates inefficient accommodation of strike-slip. Sketch of off-fault shear strain that promotes growth of the strike slip fault in the hanging wall of the reverse fault. C) Divergence of the displacement field shows extension and unclamping within the hanging wall of the first thrust fault. Median divergence from 24 - 26 mm plate displacement plotted for uncut experiments with 15˚ convergence angle (prior to dextral slip). Sketch shows the development of extension in the hanging wall of the reverse fault that unclamps any existing faults (e.g., dashed).